Fully non-linear SP_3 approximation based fluorescence optical tomography

Naren Naik*, Nishigandha Patil, Yamini Yadav, Jerry Eriksson and Asima Pradhan

In fluorescence optical tomography, many works in literature focus on the linear reconstruction problem to obtain the fluorescent yield or the linearized reconstruction problem to obtain the absorption coefficient. The nonlinear reconstruction problem, to reconstruct the fluorophore absorption coefficient, is of interest in imaging studies as it presents the possibility of better reconstructions owing to a more appropriate model. Accurate and computationally efficient forward models are also critical in the reconstruction process. The SP_N approximation to the radiative transfer equation (RTE) is gaining importance for tomographic reconstructions owing to its computational advantages over the full RTE while being more accurate and applicable than the commonly used diffusion approximation. This paper presents Gauss-Newton based fully nonlinear reconstruction for the SP_3 approximated fluorescence optical tomography problem with respect to shape as well as conventional finite-element-method (FEM) based representations. The contribution of this paper is the Frechet derivative calculations for this problem and demonstration of reconstructions in both representations. For the shape reconstructions, radial-basis-function represented level-set based shape representations are used. We present reconstructions for tumor-mimicking test objects in scattering and absorption dominant settings respectively for moderately noisy data-sets in order to demonstrate the viability of the formulation. Comparisons are presented between the non-linear and linearized reconstruction schemes in an elementwise setting illustrate the benefits of using the former especially for absorption dominant media.

Index Terms—Fluorescence tomography, Optical imaging/OCT/DOT, Image reconstruction - iterative methods

I. INTRODUCTION

The need for functional information in addition to the structural aspect becomes critical in early detection of anomalies in biomedical imaging. Fluorescence optical tomography(FOT) is

*Naren Naik is with the Department of Electrical Engineering and the Center for Lasers and Photonics, Indian Institute of Technology Kanpur, Kanpur-208016, INDIA (e-mail: nnaik@iitk.ac.in).

Nishigandha Patil is with the Department of Electrical Engineering, Indian Institute of Technology Kanpur, Kanpur-208016, INDIA (e-mail: nipat@iitk.ac.in).

Yamini Yadav is with the Department of Electronics and Communication Engineering, Babu Banarasi Das National Institute of Technology and Management, Lucknow, INDIA (e-mail: yamini.yadav123@gmail.com).

Jerry Eriksson is with the Department of Computing Science, Umeå University, S-901, 87 Umeå, SWEDEN (e-mail: jerry@cs.umu.se).

Asima Pradhan is with the Department of Physics and the Center for Lasers and Photonics, Indian Institute of Technology Kanpur, Kanpur-208016, INDIA (e-mail: asima@iitk.ac.in).

one such modality that uses the phenomenon of fluorescence to image functional/physiological as well as morphological aspects of tissue. Fluorescence optical tomography makes use of the fact that certain fluorescent dyes and proteins, upon being excited by radiation of a given wavelength (excitation wavelength) re-emit photons at another wavelength (emission wavelength). In extrinsic FOT schemes, a fluorescent dye is injected into the body, that targets specific tissue, while in intrinsic fluorescence based schemes, the fluorescence from intrinsic proteins such as NADH, associated with the onset and progression of certain diseases, such as cancer, is monitored [1], [2]. The aim of the inverse problem in FOT is to reconstruct this fluorescent source in terms of either the fluorescent yield or the fluorophore absorption coefficient. Towards this end, computationally accurate and efficient forward models are essential to improve the performance of reconstruction algorithms being developed.

The Radiative Transfer Equation (RTE) is the preferred choice for modelling propagation of optical radiation through random media [3], [4]. Of the several competing approximations to the RTE, the simplified spherical harmonics (SP_N) approximation [5] is gaining importance since it is computationally less demanding than the full radiative transfer equation [6] or its S_N [7] or P_N [8] approximations, while being more accurate and applicable than the commonly used diffusion approximation (DA) to the RTE [5], especially close to the source and boundary [9]. The advantage of using the SP_N approximation over higher order approximations (S_N and P_N) lies in the fact that one has to solve fewer coupled partial differential equations [5]. The computational advantages of using the SP_N approximation over lower order (DA) and higher order approximations (S_N and P_N) have been clearly and extensively discussed by Klose et al in their seminal paper [5]. Detailed studies, demonstrating the validity of the SP_N approximation for non-fluorescence problems, have been performed with respect to the S_N method in [5] and with respect to Monte Carlo simulations in [10]. The applicability of the SP_N approximation to model the generation and propagation of fluorescent radiation has been demonstrated by Lu et al in [11].

Several methods have been proposed in literature for obtaining fluorescence tomographic reconstructions which can be broadly classified as those that make use of linear or linearised models such as in [12]–[15] or those that use non-linear reconstruction models [16] , [17]. The linear reconstruction problem for obtaining the fluorescent yield in bioluminiscence and fluorescence tomographic problems has been solved in the SP_N approximation in frequency-domain [18], multi-spectral [12] as well as sparsely constrained [13] settings.

In [14], Lu et al have obtained linearised reconstructions for the fluorophore absorption coefficient for experimental data obtained from a mouse phantom using the SP_3 approximation. Their results illustrate the advantages of using a higher order approximation such as SP_3 for fluorescence optical tomography. As a compromise between the lower computational time afforded by DA and the improved model accuracy due to the SP_N approximation, Chen et al [19] have proposed a linear reconstruction framework in FOT using a hybrid forward model that couples the SP_N and DA. In a recent work [20], Kim et al have demonstrated non-linear reconstructions in a PDE constrained setting for frequency domain optical tomography (elastic scattering case) using the SP_3 approximation for media with non-diffuse properties wherein they quantify the advantages of using the SP_3 approximation for the non-diffuse case by comparing with the frequency domain RTE as well as DA. Their work is based on their earlier paper [21] wherein they solve the RTE based nonlinear reconstruction problem of elastic optical tomography in a PDE-constrained framework. Also, in [16], an RTE based FOT problem is solved in a PDE constrained framework. Besides the PDE-constrained framework, the non-linear reconstruction problem is also commonly approached as a least squares optimisation problem using Gauss-Newton based methods as in the present paper. Such schemes need the evaluation of the Jacobian (rather than a gradient as is the case in the PDE-constrained approaches) and the adjoint method is a popular choice for this evaluation. The adjoint method has been popularly used in literature while solving the elastic scattering problem in optical tomography [6], [22]. In a Born-approximation based linearized FOT reconstruction, adjoint based calculations for the Frechet derivatives needed for the fluorescent coupled RTE have been mentioned in [15]. In [17], Fedele et al have calculated the Frechet derivatives via an adjoint method and presented non-linear reconstructions for the FOT problem with the diffusion approximation.

In order to ameliorate the ill-posed effects of large search spaces corresponding to the unknown optical parameters in the domain of interest, typically, reconstruction schemes use the fact that the resolution needed to express the optical parameter is lower than that required for accurate representation of the optical fields. To reduce the search-space dimension as well as the effect of clutter, shape based representations capture the object(s) of interest in terms of the object-boundaries and slowly-varying/constant optical parameters. The shape based schemes typically reduce the search-space dimension by reconstructing the parameterized shape of an inhomogeneity along with typical optical-parameter values in its interior and exterior. The shape based schemes use either an explicit [23], [24], [25], [26] or an implicit [27], [28] representation for the boundary of the region(s) of interest. In the present work, as in [27], we use an implicit Hermite interpolation based radial basis function (RBF) representation of the zero level set corresponding to the boundary curve.

A fully nonlinear reconstruction scheme enables us to solve the inverse problem using the actual nonlinear forward operator; hence, we are not restricted to its linear/linearized approximations. Our present work's main contribution is to solve the fully-nonlinear SP_3-approximation modeled FOT-reconstruction problem with respect to the basic elementwise as well as level-set based shape representations. We evaluate the Frechet derivatives (Jacobians) corresponding to an SP_3-approximation modeled FOT scheme using an adjoint based framework for Gauss-Newton based reconstructions. Reconstructions are obtained in RBF-level-set represented shape-based settings as well as in a conventional elementwise object-representation. We compare the elementwise nonlinear-scheme reconstructions with those from a linearized FOT model in the spirit of [14]. Validation of the evaluated adjoint based Frechet derivatives with a finite difference scheme and preliminary results in an elementwise-reconstruction setting were reported in [29].

The problem settings and basic solution scheme are introduced in section II, and the adjoint based Frechet derivatives are presented in section III. Section IV presents the finite-element based forward problem and adjoint based Frechet derivatives. Section V details the numerical studies, and section VI has the conclusions. The appendix briefly gives the form of the Frechet derivative corresponding to the linearized problem solved.

II. PROBLEM DEFINITION

The reconstruction problem in general is to reconstruct the region of interest's optical parameters representing the fluorescent sources such as the absorption and scattering coefficients as well as the anisotropy factor from measured partial current data. The forward problem is solved to obtain measurements of either partial current or some moment of the fluence on the detector. In a practical setting, multiple source-detector configurations are used, to increase the available data, in data poor conditions. The inverse problem takes into account the experimental measurements and enables to generate an optical property map. This problem is often cast as a least squares optimisation problem. Newton type methods have been a popular choice for solving these problems [30], [12], [31], [15]. Therefore, the evaluation of Jacobian sensitivities is a vital aspect in the reconstruction process.

A. The forward model

The SP_3 approximation corresponding to a coupled system of radiative transfer equations for fluorescence propagation [12], [15] is obtained in terms of the composite Legendre moments φ [5], over a domain V as:

$$-\nabla \cdot C^{\nabla x}\nabla\varphi^x + C^x\varphi^x = 0 \tag{1a}$$

$$-\nabla \cdot C^{\nabla m}\nabla\varphi^m + C^m\varphi^m = C^\beta\varphi^x \tag{1b}$$

with partially reflecting boundary conditions,

$$C^{\nabla bx}(n.\nabla\varphi^x) + C^{bx}\varphi^x = S \tag{1c}$$

$$C^{\nabla bm}(n.\nabla\varphi^m) + C^{bm}\varphi^m = 0 \tag{1d}$$

where

$$C^{\nabla x/m} = \begin{pmatrix} \frac{1}{3\mu_{a1}^{x/m}} I & 0 \\ 0 & \frac{1}{7\mu_{a3}^{x/m}} I \end{pmatrix} C^{\beta} = \begin{pmatrix} \beta & -\frac{2}{3}\beta \\ -\frac{2}{3}\beta & \frac{4}{9}\beta \end{pmatrix}$$

$$C^{x/m} = \begin{pmatrix} \mu_{a0}^{x/m} & -\frac{2}{3}\mu_{a0}^{x/m} \\ -\frac{2}{3}\mu_{a0}^{x/m} & (\frac{4}{9}\mu_{a0}^{x/m} + \frac{5}{9}\mu_{a2}^{x/m}) \end{pmatrix}$$

$$C^{bx/m} = \begin{pmatrix} (\frac{1}{2} + A_1) & -(\frac{1}{8} + C_1) \\ -(\frac{1}{8} + C_2) & (\frac{7}{24} + A_2) \end{pmatrix}$$

$$C^{\nabla bx/m} = \begin{pmatrix} \frac{1+B_1}{3\mu_{a1}^{x/m}} & -\frac{D_1}{\mu_{a3}^{x/m}} \\ -\frac{D_2}{\mu_{a1}^{x/m}} & \frac{1+B_2}{7\mu_{a3}^{x/m}} \end{pmatrix} \quad \varphi^{x/m} = \begin{pmatrix} \varphi_1^{x/m} \\ \varphi_2^{x/m} \end{pmatrix}$$

$$C^{Sx} = \begin{pmatrix} \int_{\Omega \cdot n < 0} S(r) 2|\Omega \cdot n| d\Omega \\ \int_{\Omega \cdot n < 0} S(r)(5|\Omega \cdot n|^3 - 3|\Omega \cdot n|) d\Omega \end{pmatrix}$$

$$\underline{\nabla} = \begin{pmatrix} \frac{\partial}{\partial x} \\ \frac{\partial}{\partial y} \end{pmatrix}, \quad \nabla = \begin{pmatrix} \underline{\nabla} & 0 \\ 0 & \underline{\nabla} \end{pmatrix}, \quad I = \begin{pmatrix} 1 & 0 \\ 0 & 1 \end{pmatrix}$$

$$n = \begin{pmatrix} n_x \\ n_y \end{pmatrix}, \quad n \cdot \nabla \varphi^{(x/m)} = \begin{pmatrix} n \cdot \nabla \varphi_1^{x/m} \\ n \cdot \nabla \varphi_2^{x/m} \end{pmatrix}$$

and $\beta = \frac{\eta \mu_{af}^x}{1 - i\omega\tau}$. The absorption coefficient $\mu_a = \mu_{ai} + \mu_{af}$; μ_{ai}, μ_{af} being the chromophore and fluorophore absorption coefficient respectively with units cm^{-1}. The ability of a fluorophore to fluoresce is quantified in terms of the fluorescence quantum efficiency η and the fluorescence lifetime τ(seconds). $S(r, \Omega)$ is an external, boundary source emitting radiation at the excitation wavelength, and n denotes the outward normal at a boundary point.

The coefficients $\{A_n\}$, $\{B_n\}$, $\{C_n\}$ and $\{D_n\}$, are calculated in [5] and the absorption moments $\{\mu_{an}^{x/m}\}$ are defined as in [9], as $\mu_{an}^{x/m}(r) = \mu_t^{x/m}(r) - \mu_s^{x/m}(r)g^n + \frac{j\omega}{c}$, where g is the anisotropy factor. The system of equations 1 can be written more compactly as

$$-\underline{\nabla} \cdot C^{\nabla} \underline{\nabla} \varphi + C^{\varphi} \varphi = 0 \tag{2a}$$

$$C^{\nabla b}(\underline{n} \cdot \underline{\nabla} \varphi) + C^b \varphi = C^S \tag{2b}$$

where

$$C^{\nabla} = \begin{pmatrix} C^{\nabla x} & 0 \\ 0 & C^{\nabla m} \end{pmatrix} \qquad C^{\varphi} = \begin{pmatrix} C^x & 0 \\ -C^{\beta} & C^m \end{pmatrix}$$

$$C^{\nabla b} = \begin{pmatrix} C^{\nabla bx} & 0 \\ 0 & C^{\nabla bm} \end{pmatrix} \qquad C^b = \begin{pmatrix} C^{bx} & 0 \\ 0 & C^{bm} \end{pmatrix}$$

$$\underline{n} \cdot \underline{\nabla} \varphi = \begin{pmatrix} n \cdot \nabla \varphi^x \\ n \cdot \nabla \varphi^m \end{pmatrix} \qquad \underline{\nabla} = \begin{pmatrix} \nabla & 0 \\ 0 & \nabla \end{pmatrix}$$

$$C^S = \begin{pmatrix} C^{Sx} \\ 0 \end{pmatrix} \qquad \varphi = \begin{pmatrix} \varphi^x \\ \varphi^m \end{pmatrix} \qquad \underline{n} = \begin{pmatrix} n & 0 \\ 0 & n \end{pmatrix}$$

The exiting partial current, J^+ can be expressed in terms of the composite moments in matrix form as

$$J^{+x/m}(r_j) = C^{Jx/m} \varphi^{x/m} - C^{\nabla Jx/m} n \cdot \nabla \varphi^{x/m} \tag{3}$$

where

$$C^{Jx/m} = \begin{pmatrix} (\frac{1}{4} + J_0) & [(-\frac{2}{3})(\frac{1}{4} + J_0) + \frac{1}{3}(\frac{5}{16} + J_2)] \end{pmatrix} \delta(r - r_j),$$

$$C^{\nabla Jx/m} = \begin{pmatrix} \frac{(0.5 + J_1)}{3\mu_{a1}^{x/m}} & \frac{J_3}{7\mu_{a3}^{x/m}} \end{pmatrix} \delta(r - r_j) \text{ and the terms } \{J_i\}$$

are evaluated as in [5].

We can now write the measurement equation as

$$J^+(r_j) = C^J \varphi - C^{\nabla J} \underline{n} \cdot \underline{\nabla} \varphi \tag{4}$$

where $J^+ = \begin{pmatrix} J^{+x} \\ J^{+m} \end{pmatrix}, C^J = \begin{pmatrix} C^{Jx} & 0 \\ 0 & C^{Jm} \end{pmatrix}$ and $C^{\nabla J} = \begin{pmatrix} C^{\nabla Jx} & 0 \\ 0 & C^{\nabla Jm} \end{pmatrix}$. We note that since the amplitude and phase values of the partial current have very different scales, these need to be re-scaled. A logarithmic transformation [30] is used in our work to re-scale the measurements prior to further processing.

B. Shape representation

We can express a typical optical parameter $p(\mathbf{r})$, at a point $\mathbf{r}$ in the image space, as

$$p(\mathbf{r}) = \alpha^g(\mathbf{r}) H_\rho[s(\mathbf{r})] \tag{5}$$

where $s(.)$ is a level-set based representation of the image ([32] and references therein), with $\{\mathbf{r} : s(\mathbf{r}) = 0\}$ representing the boundary $\partial\Omega$ of the object(s) under consideration supported in region Ω; $H_\rho[.]$ is a Heaviside function taken in a suitable limiting sense [33] and the field quantity $\alpha^g(.)$ can be considered as a "ghost" parameter value manifesting itself through $H(.)$. Without loss of conceptual generality we consider $\alpha^g(\mathbf{r}) = \alpha_0$, with α_0 being a constant independent of position. In the sequel, for ease of notation, we will drop the subscript with α while denoting the constant interior value of the optical parameter.

In the present work, we use the Hermite interpolation based representation of [27]. With the objective of retaining an implicit representation coupled with significant search-space-dimensionality reduction (as in explicit schemes), we represent $s(\mathbf{r})$ as a radial basis function (RBF) via a Hermite interpolation scheme, to fit a few on-curve points (called centers of the RBF, and denoted by $\mathbf{r}_1^c \ldots \mathbf{r}_m^c$) and the normal unit vectors at those points (denoted by $\mathbf{n}_1 \ldots \mathbf{n}_m$ where $\mathbf{n}_i \equiv (cos\theta_i^c, sin\theta_i^c)$ for some θ_i^c).

We can write the level-set function as an RBF of the form

$$s(\mathbf{r}) = p(\mathbf{r}) + \sum_{j=1}^{m} \left[c_j \Phi(\mathbf{r} - \mathbf{r}_j^c) - d_j (D_{n_j}\Phi)(\mathbf{r} - \mathbf{r}_j^c) \right] \tag{6}$$

where $p(.)$ is a polynomial (typically of low order), $\Phi(.) \equiv \phi(||.||)$, with ϕ being a (usually unbounded and non-compactly supported) real valued function on $[0, \infty]$ called the basic function (chosen a twice continuously differentiable function Φ, conditionally positive definite of order k in the appropriate sense [27]), and $D_{n_j}\psi(t) \equiv \mathbf{n}_j.(\nabla\psi)(t)$ denotes the directional derivative functional w.r.t a unit normal $\mathbf{n}_j$. The coefficients c and d are the RBF coefficients.

C. The regularization problem

We can write the data equation in the discrete domain as

$$\mathbf{j}_{meas}^+ = \mathcal{A}(\mathbf{h}) \tag{7}$$

where $\mathbf{j}_{meas}^+$ is the vector of measured partial current at the detectors, and, the functional $\mathcal{A}(.)$ is the measurement operator corresponding to the tomographic process. In our work, the measurement operator is obtained via the finite element method as detailed in section IV.

For the elementwise representation, considering the FEM based discretization of the coupled fluorescence equations, the parameter vector $\mathbf{h}$ is the set of all elemental values of the optical parameter. For the shape parametrization, the parameter vector contains the coordinates of the RBF centers, the unit normals at those points, and the optical parameter inside the object (assuming an inhomogeneity with a constant value of μ_{af}^x inside). It is written as:

$$\mathbf{h} = \begin{pmatrix} \alpha \\ \mathbf{x^c} \\ \mathbf{y^c} \\ \boldsymbol{\theta^c} \end{pmatrix} \tag{8}$$

where in the two-dimensional setting considered in our work, we have as shape parameters the RBF-center coordinates $\{x_q^c | q = 1 \ldots M_p\}$, $\{y_q^c | q = 1 \ldots M_p\}$ along with the unit normals represented by the respective angles $\{\theta_q^c | q = 1 \ldots M_p\}$, corresponding in vector notation to $\mathbf{x^c}$, $\mathbf{y^c}$ and $\boldsymbol{\theta^c}$ respectively.

The basic ill-posed reconstruction problem can be defined as solving (7) for $\mathbf{h}$.

As is common practice, this problem can be solved by regularization schemes such as Tikhonov regularization or Levenberg-Marquardt schemes. A generic iteration would update a nominal estimate $\mathbf{h}$ of the unknown vector as:

$$\mathbf{h}^{new} = \mathbf{h} + \mathbf{z} \tag{9}$$

where vector $\mathbf{z}$ is evaluated as per the scheme used.

To obtain Tikhonov regularized solutions, the problem can be approximated by the following regularized nonlinear c-minimum-norm problem

$$min_{\mathbf{h}} \frac{1}{2} \left(\|\boldsymbol{\zeta}(\mathbf{h})\|^2 + \eta^2 \|\mathbf{h} - \mathbf{c}\|^2 \right) \tag{10}$$

where,

$$\boldsymbol{\zeta} = \mathbf{j}_{meas}^+ - \mathcal{A}(\mathbf{h}) \tag{11}$$

η is a regularization parameter, $\mathbf{c}$ is a known constant representing *apriori* information.

The above (regularized) c-minimum-norm problem is solved by using an iteratively regularized Gauss Newton method [25] that solves, at the current iterate $\mathbf{h}$,

$$\mathbf{z} = min_{\mathbf{q}} \left\| \begin{pmatrix} \mathbf{J}(\mathbf{h})\mathbf{q} + \boldsymbol{\zeta}(\mathbf{h}) \\ \eta(\mathbf{h} - \mathbf{c} + \mathbf{q}) \end{pmatrix} \right\|^2 \tag{12}$$

where $\mathbf{J}(\mathbf{h})$ is the Jacobian matrix of the functional $\boldsymbol{\zeta}(\mathbf{h})$ with respect to $\mathbf{h}$.

Alternatively, we can solve the ill-posed nonlinear least squares problem, $min_{\mathbf{h}} \frac{1}{2} \left(\|\boldsymbol{\zeta}(\mathbf{h})\|^2 \right)$, by the regularizing Levenberg-Marquardt (LM) scheme detailed in [34] and [35]. At each iteration the regularizing LM scheme solves the linear system of equations:

$$(\mathbf{J}^T\mathbf{J} + \eta\mathbf{L^T L})\mathbf{z} = -\mathbf{J}^T\boldsymbol{\zeta} \tag{13}$$

where η here is the Levenberg-Marquardt parameter and the matrix $\mathbf{L^T L}$ denotes the Laplacian defined similar to [30].

III. BASIC FRECHET DERIVATIVE EVALUATION

While the evaluation of the Jacobian is an important aspect of derivative-based reconstruction algorithms, it is also, often the most time-consuming section. Hence efficient methods for speeding this evaluation are essential. The evaluation of the Frechet derivative using adjoints and further vectorization of the algorithm offer tremendous improvements in speed as demonstrated by Fedele et al [17] for a diffusion based FOT problem.

To derive the Frechet derivative using the adjoint method we first define the adjoint problem, and then obtain an expression for the sensitivities from a perturbation analysis.

The adjoint problem

The adjoint solution is defined as $\Psi \equiv \begin{pmatrix} \Psi^{xx} & \Psi^{xm} \\ \Psi^{mx} & \Psi^{mm} \end{pmatrix}$, with $\Psi^{ab} = \begin{pmatrix} \Psi_1^{ab}, \\ \Psi_2^{ab} \end{pmatrix}^T$ where $a, b = x/m$, such that it solves the adjoint problem

$$-\underline{\nabla}(C^\nabla)^T \underline{\nabla}\Psi + (C^\varphi)^T\Psi = 0 \tag{14a}$$

with adjoint boundary condition

$$(C^\nabla)^T(\underline{n} \cdot \underline{\nabla}\Psi) + (C^\nabla(C^{\nabla b})^{-1}C^b)^T\Psi = C^R \tag{14b}$$

where

$$C^R = \begin{pmatrix} \Delta_d & 0 \\ 0 & \Delta_d \end{pmatrix} \tag{15}$$

with Δ_d representing the Dirac delta function at the detector positions.

Evaluating the Adjoint sensitivity

Let p denote any optical property such as μ_a, μ_s, τ etc. If we perturb p by a small amount $p \leftarrow p + \delta p$ the composite moments φ change correspondingly to $\varphi \leftarrow \varphi + \delta\varphi$. The perturbed system is:

$$-\underline{\nabla} \cdot C^\nabla(p + \delta p) - \underline{\nabla}(\varphi + \delta\varphi) + C^\varphi(p + \delta p)(\varphi + \delta\varphi) = 0 \tag{16a}$$

$$C^{\nabla b}(p + \delta p) - \underline{n} \cdot \underline{\nabla}(\varphi + \delta\varphi) + C^b(p + \delta p)(\varphi + \delta\varphi) = C^S \tag{16b}$$

We expand the perturbed terms using Taylor expansion. Using (2a) and ignoring $O(\delta^2)$ terms we get,

$$-\underline{\nabla} \cdot C^\nabla\underline{\nabla}\delta\varphi + C^\varphi\delta\varphi = \underline{\nabla} \cdot \frac{\partial C^\nabla}{\partial p}\delta p\underline{\nabla}\varphi - \frac{\partial C^\varphi}{\partial p}\delta p\varphi \tag{17a}$$

$$C^{\nabla b}\underline{n} \cdot \underline{\nabla}\delta\varphi + C^b\delta\varphi = -\frac{\partial C^{\nabla b}}{\partial p}\delta p(\underline{n} \cdot \underline{\nabla}\varphi) - \frac{\partial C^b}{\partial p}\delta p\varphi \tag{17b}$$

Now, multiplying (17a) by Ψ and integrating over the entire domain V, we get

$$\int_V \Psi^T(-\underline{\nabla} \cdot C^\nabla\underline{\nabla}\delta\varphi + C^\varphi\delta\varphi)dV$$
$$= \int_V \Psi^T(\underline{\nabla} \cdot \frac{\partial C^\nabla}{\partial p}\delta p\underline{\nabla}\varphi - \frac{\partial C^\varphi}{\partial p}\delta p\varphi)dV \tag{18}$$

Evaluating the integral on the left via integration by parts, we obtain:

$$\int_V \Psi^T(-\underline{\nabla} \cdot C^\nabla \underline{\nabla} \delta\varphi + C^\varphi \delta\varphi)dV$$

$$= \underbrace{\int_V [-\underline{\nabla} \cdot (C^\nabla)^T \underline{\nabla}\Psi + (C^\varphi)^T \Psi]^T \delta\varphi \, dV}_{=0}$$

$$+ \int_{\partial V} [(C^\nabla)^T (\underline{n} \cdot \underline{\nabla}\Psi)]^T \delta\varphi d\sigma - \int_{\partial V} \Psi^T C^\nabla (\underline{n} \cdot \underline{\nabla}\delta\varphi)d\sigma \tag{19}$$

Using the perturbed and the adjoint boundary conditions, (17b), (14b) in the above expression, we obtain,

$$\int_V \Psi^T(-\underline{\nabla} \cdot C^\nabla \underline{\nabla}\delta\varphi + C^\varphi \delta\varphi)dV$$

$$= \int_{\partial V} C^R \delta\varphi d\sigma + \int_{\partial V} \Psi^T \tilde{C}^{\nabla b} \frac{\partial C^{\nabla b}}{\partial p} \delta p \underline{n} \cdot \underline{\nabla}\varphi d\sigma$$

$$+ \int_{\partial V} \Psi^T \tilde{C}^{\nabla b} \frac{\partial C^b}{\partial p} \delta p \varphi d\sigma$$

Here $\tilde{C}^{\nabla b} = C^\nabla (C^{\nabla b})^{-1}$. Using (18) to simplify the integral on the left and (15) to simplify the first term under the integral on the right, the terms can be rearranged to write the adjoint sensitivity for the composite moments as

$$\delta\varphi = \int_V \Psi^T \underline{\nabla} \cdot \frac{\partial C^\nabla}{\partial p} \delta p \underline{\nabla}\varphi dV - \int_V \Psi^T \frac{\partial C^\varphi}{\partial p} \delta p \varphi dV$$

$$- \int_{\partial V} \Psi^T \tilde{C}^{\nabla b} \frac{\partial C^b}{\partial p} \delta p \varphi d\sigma$$

$$+ \int_{\partial V} \Psi^T \tilde{C}^{\nabla b} \frac{\partial C^{\nabla b}}{\partial p} \delta p \tilde{C}^b \varphi d\sigma \tag{20}$$

Here $\tilde{C}^b = (C^{\nabla b})^{-1} C^b$. Similarly, the perturbed measurement equation is :

$$J^+(p+\delta p) = [C^J(p+\delta p)](\varphi+\delta\varphi) - C^{\nabla J}(p+\delta p)\underline{n} \cdot \underline{\nabla}(\varphi+\delta\varphi) \tag{21}$$

Using a first order Taylor series expansion for the perturbed terms as before, ignoring $O(\delta^2)$ terms, and noting that $\frac{\partial C^J}{\partial p}, \frac{\partial C^b}{\partial p}$ equals 0, the sensitivity for the partial current is:

$$\delta J^+(p) = (C^J + C^{\nabla J} \tilde{C}^b)\delta\varphi \tag{22}$$

where $\delta J^+(p) = J^+(p + \delta p) - J^+(p)$ and δp is assumed to be negligible at the detector locations. It is worthwhile noting here, that the expression on the left in (20) can be used to obtain the sensitivity for the partial current δJ^+ directly, if the matrix C^R in (14b) is defined as $C^R = (C^J + C^{\nabla J} \tilde{C}^b)^T$ instead of using (15).

The Frechet derivatives for the frequency domain FOT problem in a linearized setting are presented in the appendix.

IV. FINITE ELEMENT FORMULATION

We use the Galerkin Finite element method (GFEM) to solve the forward and the adjoint problem. The domain V and the boundary ∂V is discretized into a structured grid with 'N_n' nodes and 'N_e' elements. We use 2D linear shape functions to approximate the composite flux φ as

$$\varphi^{x/m} \approx \hat{\varphi}^{x/m} = ([N][N]) \begin{pmatrix} [\varphi_1^{x/m}] \\ [\varphi_2^{x/m}] \end{pmatrix}$$

Here $[N(\mathbf{r})]$ for a position coordinate $\mathbf{r}$, is a nodal basis for a corresponding approximation to the optical field-quantities (φ), and $[\varphi_{1,2}^{x/m}]$ is a column vector of all the nodal values of $\varphi_{1,2}^{x/m}$. The structured grid is composed of 2D linear triangular elements. At the elemental level, the nodal basis is $[N] \equiv [N_1, N_2, N_3]$, where $N_i(\mathbf{r})$ for $i = 1, 2, 3$ are the usual 2D linear shape functions for triangular elements [36]. We denote $[\mathbf{N}] = ([N], [N])$. Quantities in $[.]$ denote the nodal values.

Forward Problem

The GFEM type weak form for the governing equations (1) with $[\mathbf{N}]$ as the test function, is:

$$\int_V [\mathbf{N}]^{\mathbf{T}}(-\nabla C^{\nabla x} \nabla \hat{\varphi}^x + C^x \hat{\varphi}^x)dV = 0 \tag{23a}$$

$$\int_V [\mathbf{N}]^{\mathbf{T}}(-\nabla C^{\nabla m} \nabla \hat{\varphi}^m + C^m \hat{\varphi}^m)dV = \int_V [\mathbf{N}]^{\mathbf{T}} C^\beta \hat{\varphi}^x dV \tag{23b}$$

Integrating the above weak form by parts, substituting the boundary conditions (as in (2b)), and introducing the approximations $\hat{\varphi}$ defined earlier, we obtain:

$$\int_V (\nabla[\mathbf{N}])^T C^{\nabla x} \nabla[\mathbf{N}][\varphi^x]dV + \int_V [\mathbf{N}]^T C^x [\mathbf{N}][\varphi^x]dV$$

$$+ \int_{\partial V} [\mathbf{N}]^T \tilde{C}^{bx}[\mathbf{N}][\varphi^x])d\sigma = \int_{\partial V} [\mathbf{N}]^T (C^{\nabla bx})^{-1} C^{Sx} d\sigma \tag{24a}$$

$$\int_V (\nabla[\mathbf{N}])^T C^{\nabla m} \nabla[\mathbf{N}][\varphi^m]dV + \int_V [\mathbf{N}]^T C^m [\mathbf{N}][\varphi^m]dV$$

$$- \int_{\partial V} [\mathbf{N}]^T \tilde{C}^{bm}[\mathbf{N}][\varphi^m])d\sigma = \int_V [\mathbf{N}]^T C^\beta [\mathbf{N}][\varphi^x]dV \tag{24b}$$

The excitation source is a point source located on the boundary. It is modeled as a delta source $S(r) = Q \cdot \delta(r - r_s)$ where r_s is the location of the point source and Q is the source strength in Wcm^{-2}. For the source term, only those nodes corresponding to the source element will be non zero, and therefore

$$\int_{\partial V} [\mathbf{N}]^T (C^{\nabla bx})^{-1} C^{Sx} d\sigma$$

$$= [\mathbf{N}(\mathbf{r_s})]^T (C^{\nabla bx})^{-1} \cdot Q \left(\frac{\int_{\Omega \cdot n < 0} 2|\Omega \cdot n|d\Omega}{\int_{\Omega \cdot n < 0} (5|\Omega \cdot n|^3 - 3|\Omega \cdot n|)d\Omega} \right)$$

The Galerkin approximation based system of equations, is thus:

$$[\mathbf{C}][\varphi] = [\tilde{\mathbf{C}}^{\mathbf{S}}] \tag{25}$$

where $[\varphi] = \begin{pmatrix} [\varphi^x] \\ [\varphi^m] \end{pmatrix}, [\mathbf{C}] = \begin{pmatrix} \mathcal{C}_x & \mathbf{0} \\ -\mathcal{M} & \mathcal{C}_m \end{pmatrix}$ and $[\tilde{\mathbf{C}}^{\mathbf{S}}] = \begin{pmatrix} [N]^T (C^{\nabla bx})^{-1} \cdot C^{Sx} \\ \mathbf{0} \end{pmatrix}$ with,

$$\mathcal{C}_{x/m} = \int_V (\nabla[\mathbf{N}])^T C^{\nabla x/m} \nabla[\mathbf{N}]dV$$

$$+ \int_V [\mathbf{N}]^T C^{x/m}[\mathbf{N}]dV + \int_{\partial V} \tilde{C}^{bx/m}[\mathbf{N}]d\sigma$$

and $\quad \mathcal{M} = \int_V [\mathbf{N}]^T C^\beta [\mathbf{N}]dV$

The partial current is obtained as

$$[J^+] = (C^J + C^{\nabla J} \tilde{C}^b)[\mathbf{N}][\varphi] \tag{26}$$

Adjoint Problem

We approximate the adjoint Ψ as

$$\Psi \approx \begin{pmatrix} \hat{\Psi}_{xx} & \hat{\Psi}_{xm} \\ \hat{\Psi}_{mx} & \hat{\Psi}_{mm} \end{pmatrix} = \left(\begin{bmatrix} \mathbf{N} \end{bmatrix} \begin{bmatrix} \mathbf{0} \end{bmatrix} \\ \begin{bmatrix} \mathbf{0} \end{bmatrix} \begin{bmatrix} \mathbf{N} \end{bmatrix} \right) \left(\begin{bmatrix} \Psi_{xx} \end{bmatrix} \begin{bmatrix} \Psi_{xm} \end{bmatrix} \\ \begin{bmatrix} \Psi_{mx} \end{bmatrix} \begin{bmatrix} \Psi_{mm} \end{bmatrix} \right)$$

The GFEM based adjoint system of equations is

$$[\tilde{\mathbf{C}}][\Psi] = [\tilde{\mathbf{C}}^{\mathbf{R}}] \tag{27}$$

where $\tilde{\mathbf{C}} = \begin{pmatrix} \tilde{\mathcal{C}}_x & -\mathcal{M}^T \\ \mathbf{0} & \tilde{\mathcal{C}}_m \end{pmatrix}$ $\tilde{\mathbf{C}}^{\mathbf{R}} = \begin{pmatrix} [\Delta_d] & [0] \\ [0] & [\Delta_d] \end{pmatrix}$ with

$$\tilde{\mathcal{C}}_{x/m} = \int_V (\nabla[\mathbf{N}])^T (C^{\nabla x/m})^T \nabla[\mathbf{N}]dV + \int_V [\mathbf{N}]^T (C^{x/m})^T [\mathbf{N}]dV$$
$$+ \int_{\partial V} (C^{\nabla x/m})^{-T} (\tilde{C}^{bx/m})^T (C^{\nabla x/m})^T [\mathbf{N}])d\sigma$$

and $[\Delta_d]$ representing the detector matrix, that is zero everywhere, except for having unity value at the detector nodes.

Frechet Derivative

The GFEM formulation for (20) is

$$[\delta\varphi] = [\Psi]^T [\delta\mathcal{C}] [\varphi] \tag{28}$$

where

$$\delta\mathcal{C} = \begin{pmatrix} \delta\mathcal{C}_x & \mathbf{0} \\ -\delta\mathcal{M} & \delta\mathcal{C}_m \end{pmatrix}$$

with $\delta\mathcal{M} = \int_V [\mathbf{N}]^T \frac{\partial C^\beta}{\partial p} \delta p[\mathbf{N}]dV$

$$\delta\mathcal{C}_{x/m} = \int_V [\nabla\mathbf{N}]^T \frac{\partial C^{x/m}}{\partial p} \delta p[\nabla\mathbf{N}]dV$$
$$- \int_V [\mathbf{N}]^T \frac{\partial C^{x/m}}{\partial p} \delta p[\mathbf{N}]dV$$
$$+ \int_{\partial V} [\mathbf{N}]^T \tilde{C}^{\nabla bx/m} \frac{\partial C^{\nabla bx/m}}{\partial p} \delta p \tilde{C}^{bx/m}[\mathbf{N}]d\sigma$$
$$- \int_{\partial V} [\mathbf{N}]^T \tilde{C}^{\nabla bx/m} \frac{\partial C^{bx/m}}{\partial p} \delta p[\mathbf{N}]d\sigma$$

The variation in the composite moments can thus be written as:

$$[\delta\varphi] = \mathbf{J}_\varphi \delta\mathbf{p} \tag{29}$$

where $\delta\mathbf{p}$ denotes the vector of elemental perturbations of the optical parameter, and $\mathbf{J}_\varphi$ represents the corresponding Jacobian matrix.

The FEM formulation for the sensitivity of the partial current is thus:

$$[\delta J^+] = (C^J + C^{\nabla J}\tilde{C}^b)[\delta\varphi] \equiv \mathbf{J}_p\delta\mathbf{p} \tag{30}$$

where $\mathbf{J}_p(= (C^J + C^{\nabla J}\tilde{C}^b)\mathbf{J}_\varphi)$ denotes the Jacobian corresponding to the first variation of the partial current with respect to the elemental vector of the optical parameter $\mathbf{p}$.

Note: If $\tilde{\mathbf{C}}^{\mathbf{R}} = [(\mathbf{C}^{\mathbf{J}} + \mathbf{C}^{\nabla\mathbf{J}}\tilde{\mathbf{C}}^{\mathbf{b}})]$, then $\delta J^+ = [\Psi]^T[\delta\mathcal{C}][\varphi] \equiv \mathbf{J}_p\delta\mathbf{p}$

Further, for shape reconstructions, having defined our unknown in (8) as $\mathbf{h} = \left(\alpha, \mathbf{x}^{\mathbf{c}T}, \mathbf{y}^{\mathbf{c}T}, \boldsymbol{\theta}^{\mathbf{c}T} \right)^T$, we can write the

first variation of the elemental vector $\mathbf{p}$ with respect to the shape parameters as:

$$\delta\mathbf{p} = H_\rho[\mathbf{s}]\delta\alpha + \alpha diag(H'_\rho[\mathbf{s}])\delta\mathbf{s} \tag{31}$$

where $\mathbf{s}$ is the vector of level-set values taken at the centroids of the mesh-elements.

Now, the first variation of the level-set values $\delta\mathbf{s}$ with respect to the coordinates of the RBF centers and the normals at those points can be written symbolically as:

$$\delta\mathbf{s} = \mathbf{J}_c \begin{pmatrix} \delta\mathbf{x}^c \\ \delta\mathbf{y}^c \\ \delta\boldsymbol{\theta}^c \end{pmatrix} \tag{32}$$

where the explicit form of the Jacobian matrix $\mathbf{J}_c$ is given in [27] and is not repeated here for the sake of brevity.

Hence, we can now write:

$$[\delta J^+] = \mathbf{J}_p \left(H_\rho[\mathbf{s}] \quad \alpha diag(H'_\rho[\mathbf{s}])\mathbf{J}_c \right) \delta\mathbf{h} \equiv \mathbf{J}_h\delta\mathbf{h} \tag{33}$$

with $\mathbf{J}_h(\equiv \mathbf{J}_p \begin{bmatrix} H_\rho[\mathbf{s}] & \alpha diag(H'_\rho[\mathbf{s}])\mathbf{J}_c \end{bmatrix})$ being the Jacobian matrix corresponding to the variation of the measured partial currents with respect to the shape-based-unknown vector, $\mathbf{h}$.

V. NUMERICAL STUDIES

In this study, two kinds of settings were considered, the first for a scattering dominated medium and the second, for an absorption dominated medium, with square domains of sizes $2\text{cm} \times 2\text{cm}$ and $1\text{cm} \times 1\text{cm}$ respectively. In the first setting the optical properties for the phantom were chosen to mimic an actual tissue sample as in [17]. The extrinsic fluorophore considered is indocyanine green (ICG) with excitation wavelength, $\lambda_x = 785\text{nm}$ and emission at $\lambda_m = 830\text{nm}$. In the second setting, the optical properties for the phantom are chosen as in [18]. The extrinsic fluorophore considered in this case is Qdot ®565 [37] with excitation peak at $\lambda_x = 300\text{nm}$ and emission at $\lambda_m = 565\text{nm}$. This choice of wavelengths (for excitation and emission) as well as the optical parameters enables us to investigate a setting wherein the diffusion approximation is clearly not valid (we have also verified this via comparison with Monte Carlo results for the given excitation wavelength). The optical properties for both the settings are listed in Table I and the anisotropy factor g is taken to be 0.8 in all cases.

An excitation source of strength $1\text{mW}/\text{cm}^{-2}$ and modulated at a frequency of 100 MHz is placed at the centre of each side of the square domain sequentially. Nineteen equispaced detectors are placed on each side of the phantom that measure the fluorescent emission. In each setting, we consider two kinds of phantoms, one with a bean shaped concave inhomogeneity (CS or CA resp.), and the other with two square objects (DS or DA resp.).

Our SP_3 codes have been validated with respect to Monte Carlo simulations for homogeneous media with and without fluorescence as well as heterogeneous media with fluorescence. The Monte Carlo codes used by us for verification are open source codes available at http://omlc.org/software/mc/.

In Fig.1 we plot maps of the sensitivity for phantoms DS, DA and DA2; where, DA2 denotes an absorption-dominant

TABLE I

DESCRIPTION OF THE PHANTOMS AND THE FLUOROPHORES FOR BOTH THE GROUPS OF SIMULATIONS. $\mu_a(\text{cm}^{-1})$ AND $\mu_{rs}(\text{cm}^{-1})$ ARE THE ABSORPTION AND SCATTERING COEFFICIENTS RESPECTIVELY. η IS THE FLUORESCENT QUANTUM YIELD AND τ IS THE FLUORESCENCE LIFETIME FOR THE FLUOROPHORE. THE SUBSCRIPTS i/f DENOTE QUANTITIES RELATED TO THE BACKGROUND AND FLUOROPHORE AND THE SUPERSCRIPTS x/m INDICATE QUANTITIES AT EXCITATION/EMISSION WAVELENGTH RESPECTIVELY.

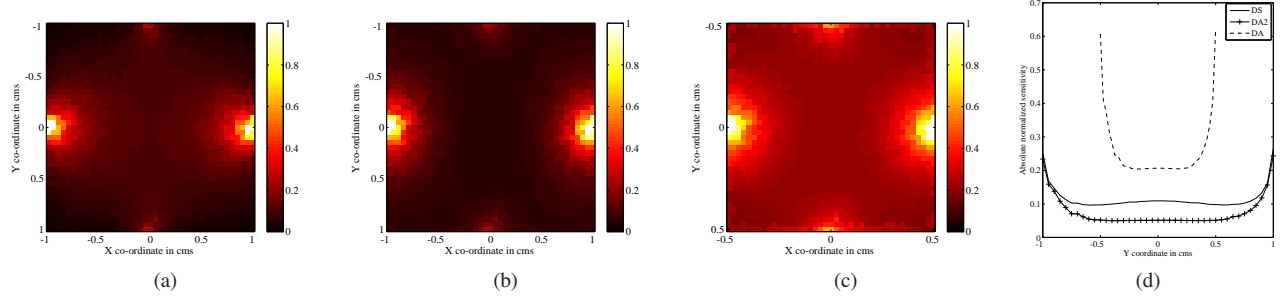|	μ_{ai}^x	μ_{af}^x	μ_{ai}^m	μ_{af}^m	μ_{rs}^x	μ_{rs}^m	η_f	$\tau_f(\text{ns})$
Phantom 1	0.031	0.006	$0.7987\mu_{ai}^x$	$0.0846\mu_{af}^x$	10.95	$0.732\mu_{rs}^x$	0.016	0.56
Phantom 2	0.45	0.087	0.45	$0.043\mu_{af}^x$	2.0	2.0	0.019	0.4

Fig. 1. Maps of absolute value of the normalized sensitivity for a phantom with two square inhomogeneities in different settings:(a)Scattering dominant medium with domain size 2cm × 2cm (DS); (b) Absorption dominant medium with domain size 2cm × 2cm (DA2); (c) Absorption dominant medium with domain size 1cm × 1cm (DA); (d) Cross sectional plot of absolute values of normalized sensitivity for a phantom with two square inhomogeneites in different settings along $x = 0$.

phantom, which is of dimension 2cm × 2cm and has a double-square inhomogeneity. It is observed that in the absorption-dominant setting, the sensitivity values in the central region are very low for a large domain (2cm × 2cm) (refer Fig.1(b) and (d)). This presents a limitation to the reconstruction algorithms for such larger domains in predominantly absorbing media and the reconstructions are prone to artifacts in regions of very low sensitivity. Hence a smaller domain size (1cm × 1cm, Fig.1 (c)) is considered for this setting.

The Frechet derivatives have been validated by comparison of the adjoint based calculated values with those obtained from a finite-difference calculation in our earlier work [29]. The computation of the sensitivities on a structured grid with 3200 elements requires 3 seconds (on average) using the adjoint approach (with a vectorized implementation detailed in [17]) and 940 seconds (on average) using the finite difference method in MATLAB on a system powered by the Intel Xeon(R) processor. This huge speedup (313 times) in the evaluation of the Frechet derivatives justifies the use of the adjoint method for such problems.

Reconstruction results are presented using two regularization schemes. A regularizing Levenberg-Marquardt (LM) method [34] is used for the elementwise reconstructions and an iteratively regularized "c-minimum-norm" Tikhonov scheme [25], [27] is used for the small scale RBF-level-set based shape based reconstructions with the vector **c** acting as prior information. The LM scheme being a "no-prior" method, is used by us to obtain element-wise reconstructions wherein we assume a very rudimentary initialization of a homogeneous medium of absorption coefficient 0.001cm^{-1} for all phantoms. Comparisons between the linearized and non-linear reconstructions are also presented in an element-wise framework.

In order to quantify the quality of reconstructions we utilize two criteria [38], [39]: (a) a normalized mean square error of the area-parameter product; parameter here referring to the optical parameter of absorption-coefficient-difference (w.r.t the background) $i.e. \mu_{af}^x$, and, (b) the distance of the centroid(s) of feature(s) of interest in the image. In addition, only for the shape reconstructions we also measure the normalized absolute error of the optical parameter reconstructed. These error metrics are defined in Table II.

The area and centroid coordinates are evaluated by discretizing the reconstructed/actual images, and are defined as:

$$A_{object} = \sum_{i,j} \chi_{object}(x_i, y_j) \tag{34}$$

$$\overline{x}_{object} = \frac{\sum_{i,j} x_i \chi_{object}(x_i, y_j)}{A_{object}}, \quad \overline{y}_{object} = \frac{\sum_{i,j} y_i \chi_{object}(x_i, y_j)}{A_{object}} \tag{35}$$

where the indices (i, j) represent the x and y-indices of the triangle centroids and range over the extent of the discretized image, and $\chi_{object}(.)$ is the characteristic function with respect to the object support.

Reconstructions are shown for three moderately noisy data sets for each phantom in each setting, and corresponding error measures obtained are tabulated in Table III.

In the figures, the actual object is shown in dashed (green) lines and shape reconstructions are depicted as solid (red) lines. The nonlinear reconstructions are characterized by their gray-scale map and the linearized ones are represented only in terms of their spatial extent with a wire-frame. For the reconstructed optical parameter (μ_{af}^x), Table IV gives the shape-reconstructed value, as well as only the peak values obtained from the elementwise linearized and nonlinear reconstructions.

TABLE II

DEFINITIONS OF THE MEASURES USED TO QUANTIFY THE ELEMENT-WISE AND SHAPE RECONSTRUCTIONS. α DENOTES THE OPTICAL PARAMETER, A THE AREA OF THE OBJECT AND (x, y) ARE THE CENTROID COORDINATES. THE SUPERSCRIPTS 'rec' AND 'ac' ARE USED TO DENOTE THE RECONSTRUCTED AND ACTUAL QUANTITIES RESPECTIVELY. FOR THE ELEMENT-WISE CASE, i RELATES TO THE i-TH ELEMENT.

Measure	Element-wise	Shape
Area-parameter product	$E_a = \frac{\left\| \sum_i (\alpha_i^{rec} A_i) - \sum_i (\alpha_i^{ac} A_i) \right\|}{\sum_i \left\| \alpha_i^{ac} A_i \right\|} \times 100\%$	$E_a = \frac{\left\| \alpha_{rec} A_{rec} - \alpha_{ac} A_{ac} \right\|}{\left\| \alpha_{ac} A_{ac} \right\|} \times 100\%$
Euclidean distance	$E_c = \sqrt{(\overline{x}^{rec} - \overline{x}^{ac})^2 + (\overline{y}^{rec} - \overline{y}^{ac})^2}$	$E_c = \sqrt{(\overline{x}^{rec} - \overline{x}^{ac})^2 + (\overline{y}^{rec} - \overline{y}^{ac})^2}$
Normalized absolute error	Not applicable	$E_\alpha = \frac{\left\| \alpha^{rec} - \alpha^{ac} \right\|}{\left\| \alpha^{ac} \right\|} \times 100\%$

TABLE III

ERROR MEASURES FOR SHAPE AND ELEMENTWISE RECONSTRUCTIONS; FOR RESPECTIVE SET A, S, C∗-N1, C∗-N2 AND C∗-N3 DENOTE THE CONCAVE PHANTOM DATA WITH NOISE LEVELS N1,N2 AND N3 RESPECTIVELY, AND D∗-N1, D∗-N2 AND D∗-N3 DENOTE THE DATA FOR THE DOUBLE PHANTOM; E_a, E_c AND (ONLY FOR SHAPE RECONSTRUCTIONS) E_α DENOTE THE AREA-PARAMETER-PRODUCT, CENTROID, AND OPTICAL-PARAMETER ERROR MEASURES RESPECTIVELY; $E_c = (E_{c1}, E_{c2})$ CORRESPONDING TO THE TWO OBJECTS (ASSOCIATED WITH $y < 0$ AND $y > 0$ RESPECTIVELY) FOR THE DOUBLE PHANTOMS

	Noise-level (dB)	$E_a\%$(element)		$E_a\%$ (shape)	E_c(mm)(element)		E_c (mm) (shape)	$E_\alpha\%$(shape)
		linearized	non-linear		linearized	non-linear		
				Scattering-dominant setting				
CS-N1	34.49	0.58	4.34	0.12	0.424	0.257	0.021	2.75
CS-N2	28.43	3.21	1.61	1.13	0.438	0.262	0.016	5.65
CS-N3	25.18	4.87	0.57	0.67	0.467	0.187	0.008	11.79
DS-N1	35.62	8.39	7.38	0.55	(0.094,0.480)	(0.209,0.584)	(0.101,0.288)	19.62
DS-N2	28.64	13.77	11.75	0.46	(0.030,0.102)	(0.171,0.191)	(0.148,0.159)	8.50
DS-N3	23.25	7.61	5.67	0.32	(0.252,0.327)	(0.178,0.095)	(0.082,0.373)	8.52
				Absorption-dominant setting				
CA-N1	34.81	50.88	51.86	0.50	0.369	0.099	0.007	0.50
CA-N2	28.96	50.82	52.42	0.09	0.374	0.071	0.033	4.59
CA-N3	22.59	51.28	55.40	1.31	0.327	0.153	0.022	8.36
DA-N1	35.20	10.03	2.79	0.14	(0.245,0.234)	(0.093,0.114)	(0.028,0.028)	20.08
DA-N2	28.68	18.47	3.00	0.94	(0.181,0.118)	(0.147,0.261)	(0.212,0.039)	2.80
DA-N3	23.00	26.99	13.16	1.03	(0.180,0.099)	(0.195,0.125)	(0.216,0.052)	24.49

TABLE IV

RECONSTRUCTED OPTICAL PARAMETER VALUE IN THE SCATTERING-DOMINANT(CS, DS) AND ABSORPTION-DOMINANT (CA, DA) SETTINGS FOR THE ELEMENTWISE AS WELL AS SHAPE RECONSTRUCTIONS. IN THE ELEMENTWISE SETTING, THE PARAMETER VALUES TABULATED CORRESPOND TO THE MAXIMUM VALUE OF THE OPTICAL PARAMETER WITHIN THE REGION OF INTEREST

Data-set	Element-wise		Shape
	linearized	non-linear	
Scattering-dominant setting, $\mu_{af,true}^x = 0.006\text{cm}^{-1}$			
CS-N1	0.0032	0.0044	0.0061
CS-N2	0.0029	0.0034	0.0063
CS-N3	0.0028	0.0051	0.0053
DS-N1	0.0039	0.0053	0.0048
DS-N2	0.0042	0.0055	0.0055
DS-N3	0.0056	0.0053	0.0055
Absorption-dominant setting, $\mu_{af,true}^x = 0.087\text{cm}^{-1}$			
CA-N1	0.0376	0.0639	0.0866
CA-N2	0.0372	0.0624	0.0830
CA-N3	0.0377	0.0719	0.0797
DA-N1	0.0619	0.0760	0.1045
DA-N2	0.0576	0.0711	0.0846
DA-N3	0.0569	0.0825	0.0657

A. Reconstruction results in scattering-dominant setting

Fig.2(a,c,e) and Fig.2(b,d,f) show the reconstructions obtained for the single concave phantom and double square phantom cases respectively.

The linearized as well as non-linear reconstructions of optical parameter (μ_{af}^x) in the elementwise setting are plotted after thresholding the reconstructed $\mu_{af}^{x,rec}$ at $0.2max(\mu_{af}^{x,rec})$. In the elementwise setting, we initialise the fluorophore absorption coefficient to be homogeneous with value 0.001cm^{-1} for both the phantoms. In both, the single phantom (CS), as well as the double phantom reconstructions (DS), the centroid error (E_c) observed is low, demonstrating the effectiveness of the regularizing LM reconstruction scheme in localizing the objects. We also observe that in the scattering dominant case the linearized reconstruction scheme performs at par with the non-linear reconstruction scheme in terms of the error metrics (see Table III), however the non-linear scheme consistently outperforms the linearized reconstruction scheme in terms of the peak parameter value estimated (see Table IV). In the double phantom reconstructions, artifacts are observed very close to the boundary and also close to the center. These are of considerably low value and small extent.
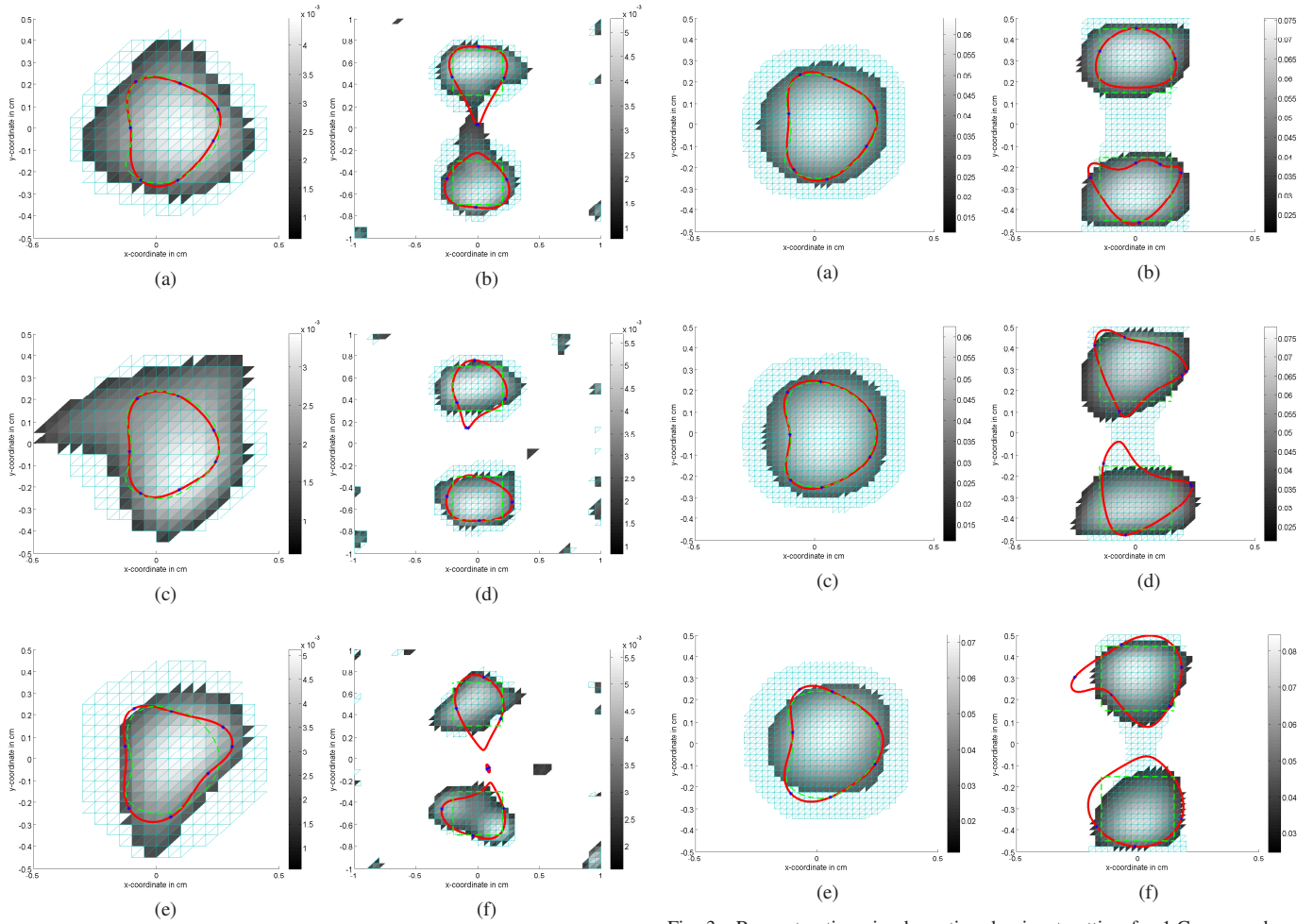
Fig. 2. Reconstructions in scattering-dominant setting for 1.Concave phantom (a) data-set CS-N1, (c) data-set CS-N2 and (e) data-set CS-N3 and 2.Double phantom (b) data-set DS-N1, (d) data-set DS-N2 and (f) data-set DS-N3. In the figure, comparisons are presented between the true object (bright green-dashed line) and (i) non-linear reconstructions in an element-wise setting (solid-grayscale) (ii) linearized reconstructions in an element-wise setting (wire frame) and (iii)RBF-level-set based shape reconstructions (red, solid line).

Fig. 3. Reconstructions in absorption-dominant setting for 1.Concave phantom (a) data-set CA-N1 , (c) data-set CA-N2 and (e) data-set CA-N3 and 2.Double phantom (b) data-set DA-N1 , (d) data-set DA-N2 and (f) data-set DA-N3. In the figure, comparisons are presented between the true object (bright green-dashed line) and (i) non-linear reconstructions in an element-wise setting (solid-grayscale) (ii) linearized reconstructions in an element-wise setting (wire frame) and (iii)RBF-level-set based shape reconstructions (red, solid line).

For the shape reconstructions, we initialise the single phantom reconstructions by a circular object of radius 0.4cm (of the order of twice the actual object size, as is also observable from the elementwise reconstructions) and absorption coefficient $0.001\mathrm{cm}^{-1}$. The double phantom reconstructions were initialised by a single circular object of radius 0.5 cm and absorption coefficient $0.001\mathrm{cm}^{-1}$; the reconstructed iterates obtained see the split of the single-phantom initial estimate into two distinct objects. The results shown for the shape reconstructions in Fig. 2 show a clear localization and good optical parameter reconstructions, which are evident from the low centroid and parameter errors in both the single phantom and double phantom reconstructions, and also from Table IV. In addition, the single concave phantom's concavity, which is the salient shape feature of the phantom, is well captured.

B. Reconstruction results in absorption-dominant setting

Fig.3(a,c,e) and Fig.3(b,d,f) show the reconstructions obtained for the single concave phantom and double square phantom cases respectively. The linearized as well as non-linear reconstructions of optical parameter (μ_{af}^{x}) in the elementwise setting are plotted after thresholding the reconstructed $\mu_{af}^{x,rec}$ at $0.3max(\mu_{af}^{x,rec})$. In the elementwise setting, we initialise the fluorophore absorption coefficient to be homogeneous with value $0.001\mathrm{cm}^{-1}$ for both the phantoms. For the concave phantom, the low centroid errors in the elementwise setting too indicate that the object is reasonably well localized though spread out in extent. For this case, the linearized reconstruction scheme underestimates the parameter value as compared to the non-linear scheme. However the area-parameter product (E_a) measure for both the schemes is similar since in the linearized reconstructions, the underestimated parameter value is compensated by an overestimation of the spatial extent of the reconstructed object. In the double phantom case, while

with the non-linear scheme a distinct split is obtained between the two objects, it is not so in the linearized scheme. As with concave phantom, in this case too the peak parameter value is underestimated by the linearized scheme with higher values of $\mu_{af}^{x,rec}$ very close to the boundary. The reconstructions in the double phantom case are more sensitive to the initial estimate.

The shape reconstructions are also able to clearly resolve the two square-shaped inhomogeneities. The iteratively regularized scheme is started with a single circular object of radius about 0.4 cm of absorption coefficient of about 0.015cm^{-1} and it converges to the two-objects. The absorption coefficients are also very well reconstructed with values given in Table IV. The single-concave-object's reconstructions show a good reconstruction of the concavity as well as the absorption coefficient as is seen in Fig.3 and further quantified by the values of E_a, E_c and E_α in Table III. This further underscores the utility of the shape-reconstructions with of course the underlying assumptions.

We observe that the nonlinear reconstruction scheme performs better than the linearized one in terms of the maximum parameter value estimated, as well as in capturing the actual spatial support of the object. These benefits of using a non-linear reconstruction over a linearized reconstruction are highlighted in the absorption dominant setting since the errors due to not considering the full adjoint sensitivity (as in the non-linear scheme) but only an approximation to it (as in the linearized scheme) are significant when the value of the fluorophore absorption coefficient is large. These observations are consistent with those presented by Eppstein et al in [40].

In our simulations, we observe that with the non-linear reconstruction scheme in the elementwise as well as shape based settings, stable results are obtained upto about SNRs of 25 dB in both the scattering and absorption dominant settings. As the SNRs go down to about 20dB, reconstructions can be obtained but they are unstable and often diverge rapidly after the appropriate regularization-parameter/reconstruction is reached. For these low SNRs, we observe that at these points of "correct" regularization parameter, the data residual is quite large, which tells us that we are obtaining a reasonable reconstruction by avoiding overfitting the data. Hence, we only present the results of the moderately noisy cases.

VI. CONCLUSIONS

This paper presents Gauss-Newton based fully nonlinear reconstructions for the SP_3 approximated fluorescence optical tomography problem with respect to level-set shape-based as well as conventional elementwise (in a finite element framework) representations. The contribution of this paper is the Frechet derivative calculations for this problem and demonstration of non-linear reconstructions with both representations. We present reconstructions of tumor-mimicking phantoms in scattering as well as absorption dominant settings in two dimensions for moderately noisy data sets. Comparison of the nonlinear reconstructions with those obtained from a linearized FOT reconstruction in an elementwise setting demonstrate better localization of the object as well as estimation of the optical parameter with the nonlinear scheme.

The elementwise reconstructions carried out using the regularizing Levenberg-Marquardt method start with practically no prior information and give the necessary support information to start the shape reconstructions. The significantly reduced errors in area-parameter product, the object centroid, as well as the reconstructed optical parameter, show the improvement in localization as well as parameter-reconstruction of the shape-based scheme over the elementwise reconstructions. The results obtained demonstrate the viability of the SP_3-modeled fully nonlinear reconstructions for fluorescence optical tomography.

The demonstrated scheme is scalable to three dimensions. In a 3D framework, in order to retain the efficacy of the adjoint based evaluation of the Frechet derivative, the source-detector configuration needs to be optimized; this is the subject of ongoing study.

APPENDIX
FRECHET DERIVATIVE FOR THE LINEARIZED PROBLEM

To linearize the SP_3 forward model, it is assumed (as in [14]) that the contribution of the fluorophore absorption coefficient, $\mu_{af}^{x/m}$ to the total absorption coefficient $\mu_a^{x/m}$ is small. Hence, perturbations in the system matrices $C^{\nabla x/m}, C^{x/m}, C^{\nabla bx/m}$ and $C^{bx/m}$ due to perturbations in $\mu_{af}^{x/m}$ are neglected. Incorporating these assumptions, the expression for the sensitivity of the composite moments with respect to μ_{af}^x given by (20) reduces to:

$$\delta\varphi^m = \int_V \Psi_{mm}^T C^\beta \varphi^x dV \tag{36}$$

In [40] this is referred to as the approximate adjoint sensitivity. In the same paper a detailed comparison of reconstructions of μ_{af}^x with the exact and approximate adjoint sensitivities for the diffusion approximation has also been presented. The approximate sensitivity for partial current at the emission wavelength can now be written as,

$$\delta J^{+m} = (C^{Jm} + C^{\nabla Jm}\tilde{C}^{bm})\delta\varphi^m \tag{37}$$

REFERENCES

[1] V. Ntziachristos, "Fluorescence molecular imaging," Annual Review of Biomedical Engineering, vol. 8, no. 1, pp. 1–33, 2006, pMID: 16834550.

[2] N. Thekkek and R. Richards-Kortum, "Optical imaging for cervical cancer detection: solutions for a continuing global problem," Nature Reviews Cancer, vol. 8, no. 9, pp. 725–731, 2008.

[3] A. Ishimaru, Wave propagation and scattering in random media. Academic press New York, 1978, vol. 2.

[4] S. Chandrasekhar, Radiative transfer. Courier Corporation, 2013.

[5] A. D. Klose and E. W. Larsen, "Light transport in biological tissue based on the simplified spherical harmonics equations," J. Comput. Phys., vol. 220, no. 1, pp. 441–470, dec 2006.

[6] S. R. Arridge, "Optical tomography in medical imaging," Inverse problems, vol. 15, no. 2, p. R41, 1999.

This article has been accepted for publication in a future issue of this journal, but has not been fully edited. Content may change prior to final publication. Citation information: DOI 10.1109/TMI.2017.2718028, IEEE Transactions on Medical Imaging

11

[7] C. Siewert, "A discrete-ordinates solution for radiative-transfer models that include polarization effects," Journal of Quantitative Spectroscopy and Radiative Transfer, vol. 64, no. 3, pp. 227–254, 2000.

[8] K. M. Case and . Zweifel, Paul Frederick, Linear transport theory. Reading, Mass. : Addison-Wesley Pub. Co, 1967.

[9] M. Chu, K. Vishwanath, A. D. Klose, and H. D. and, "Light transport in biological tissue using three-dimensional frequency-domain simplified spherical harmonics equations," Physics in medicine and biology, vol. 54, no. 8, p. 2493, 2009.

[10] M. Chu, "Modelling light transport through biological tissue using the simplified spherical harmonics approximation," 2010.

[11] Y. Lu, B. Zhu, H. Shen, J. C. Rasmussen, G. Wang, and E. M. Sevick-Muraca, "A parallel adaptive finite element simplified spherical harmonics approximation solver for frequency domain fluorescence molecular imaging," Physics in medicine and biology, vol. 55, no. 16, p. 4625, 2010.

[12] A. D. Klose and T. Pöschinger, "Excitation-resolved fluorescence tomography with simplified spherical harmonics equations," Physics in medicine and biology, vol. 56, no. 5, p. 1443, 2011.

[13] D. Han, J. Tian, K. Liu, J. Feng, B. Zhang, X. Ma, and C. Qin, "Sparsity-promoting tomographic fluorescence imaging with simplified spherical harmonics approximation," IEEE Transactions on Biomedical Engineering, vol. 57, no. 10, pp. 2564–2567, 2010.

[14] Y. Lu, B. Zhu, C. Darne, I.-C. Tan, J. C. Rasmussen, and E. M. Sevick-Muraca, "Improvement of fluorescence-enhanced optical tomography with improved optical filtering and accurate model-based reconstruction algorithms," Journal of biomedical optics, vol. 16, no. 12, pp. 126 002–1 260 024, 2011.

[15] A. Joshi, J. C. Rasmussen, E. M. Sevick-Muraca, T. A. Wareing, and J. McGhee, "Radiative transport-based frequency-domain fluorescence tomography," Physics in medicine and biology, vol. 53, no. 8, p. 2069, 2008.

[16] H. K. Kim, J. H. Lee, and A. H. Hielscher, "Pde-constrained fluorescence tomography with the frequency-domain equation of radiative transfer," Selected Topics in Quantum Electronics, IEEE Journal of, vol. 16, no. 4, pp. 793–803, 2010.

[17] F. Fedele, J. P. Laible, and M. J. Eppstein, "Coupled complex adjoint sensitivities for frequency-domain fluorescence tomography: Theory and vectorized implementation," J. Comput. Phys., vol. 187, no. 2, pp. 597–619, May 2003.

[18] H. Guo, Y. Hou, X. He, J. Yu, J. Cheng, and X. Pu, "Adaptive hp finite element method for fluorescence molecular tomography with simplified spherical harmonics approximation," Journal of Innovative Optical Health Sciences, vol. 7, no. 02, p. 1350057, 2014.

[19] X. Chen, F. Sun, D. Yang, and J. Liang, "Coupled third-order simplified spherical harmonics and diffusion equation–based fluorescence tomographic imaging of liver cancer," Journal of biomedical optics, vol. 20, no. 9, pp. 090 502–090 502, 2015.

[20] H. K. Kim, L. D. Montejo, J. Jia, and A. H. Hielscher, "Frequency-domain optical tomographic image reconstruction algorithm with the simplified spherical harmonics (sp3) light propagation model," International Journal of Thermal Sciences, vol. 116, pp. 265 – 277, 2017. [Online]. Available: http://www.sciencedirect.com/science/article/pii/S1290072916309887

[21] H. K. Kim and A. H. Hielscher, "A pde-constrained sqp algorithm for optical tomography based on the frequency-domain equation of radiative transfer," Inverse Problems, vol. 25, no. 1, p. 015010, 2009.

[22] K. Ren, G. Bal, and A. H. Hielscher, "Frequency domain optical tomography based on the equation of radiative transfer," SIAM Journal on Scientific Computing, vol. 28, no. 4, pp. 1463–1489, 2006.

[23] M. E. Kilmer, E. L. Miller, A. Barbaro, and D. Boas, "Three-dimensional shape-based imaging of absorption perturbation for diffuse optical tomography," Appl. Opt., vol. 42, no. 16, pp. 3129–3144, Jun 2003.

[24] A. D. Zacharopoulos, S. R. Arridge, O. Dorn, V. Kolehmainen, and J. Sikora, "Three-dimensional reconstruction of shape and piecewise constant region values for optical tomography using spherical harmonic parametrization and a boundary element method," Inverse Problems, vol. 22, no. 5, p. 1509, 2006.

[25] N. Naik, J. Eriksson, P. De Groen, and H. Sahli, "A nonlinear iterative reconstruction and analysis approach to shape-based approximate electromagnetic tomography," Geoscience and Remote Sensing, IEEE Transactions on, vol. 46, no. 5, pp. 1558–1574, 2008.

[26] N. Hyvönen, "Fréchet derivative with respect to the shape of a strongly convex nonscattering region in optical tomography," Inverse Problems, vol. 23, no. 5, p. 2249, 2007.

[27] N. Naik, R. Beatson, J. Eriksson, and E. van Houten, "An implicit radial basis function based reconstruction approach to electromagnetic shape tomography," Inverse Problems, vol. 25, no. 2, p. 025004, 2009.

[28] A. Aghasi, M. Kilmer, and E. L. Miller, "Parametric level set methods for inverse problems," SIAM Journal on Imaging Sciences, vol. 4, no. 2, pp. 618–650, 2011.

[29] N. Patil, N. Naik, Y. Yadav, and A. Pradhan, "An sp3-approximation based fully non-linear reconstruction scheme for fluorescence optical tomography," in 12th International Conference on Fiber Optics and Photonics. Optical Society of America, 2014, p. T2B.4.

[30] M. Schweiger, S. R. Arridge, and I. Nissilä, "Gauss–newton method for image reconstruction in diffuse optical tomography," Physics in medicine and biology, vol. 50, no. 10, p. 2365, 2005.

[31] M. Chu and H. Dehghani, "Image reconstruction in diffuse optical tomography based on simplified spherical harmonics approximation," Optics express, vol. 17, no. 26, pp. 24 208–24 223, 2009.

[32] F. Santosa, "A level-set approach for inverse problems involving obstacles," ESAIM: Control, Optimisation and Calculus of Variations, vol. 1, pp. 17–33, 1996.

[33] T. F. Chan and L. A. Vese, "Active contours without edges," Image processing, IEEE transactions on, vol. 10, no. 2, pp. 266–277, 2001.

[34] A. Doicu, T. Trautmann, and F. Schreier, Numerical regularization for atmospheric inverse problems. Springer Science & Business Media, 2010.

[35] M. Hanke, "A regularizing levenberg-marquardt scheme, with applications to inverse groundwater filtration problems," Inverse problems, vol. 13, no. 1, p. 79, 1997.

[36] J.-M. Jin, The finite element method in electromagnetics. John Wiley & Sons, 2014.

[37] T. Scientific, "Qdot Ⓡ565 streptavidin conjugate, product catalog," https://www.thermofisher.com/order/catalog/product/Q10131MP.

[38] N. Naik, R. Beatson, J. Eriksson, and E. van Houten, "An implicit radial basis function based reconstruction approach to electromagnetic shape tomography," Inverse Problems, vol. 25, no. 2, p. 025004, 2008.

[39] T. Lucas, "A pde-based inverse solver for diffusion tomography using multiple continuous wave sources," Inverse Problems in Science and Engineering, vol. 16, no. 1, pp. 109–126, 2008.

[40] M. J. Eppstein, F. Fedele, J. Laible, C. Zhang, A. Godavarty, and E. M. Sevick-Muraca, "A comparison of exact and approximate adjoint sensitivities in fluorescence tomography," IEEE Transactions on Medical Imaging, vol. 22, no. 10, pp. 1215–1223, 2003.